

# Purely Spin-Vibronic Coupling Assisted Triplet to Singlet Up-Conversion for Real Deep Blue Organic Light-Emitting Diodes with Over 20% Efficiency and $y$ Color Coordinate of 0.05

Vilas Venunath Patil, Ha Lim Lee, Inkoo Kim, Kyung Hyung Lee, Won Jae Chung, Joonghyuk Kim, Sangho Park, Hyeonho Choi, Won-Joon Son, Soon Ok Jeon,\* and Jun Yeob Lee\*

Finding narrow-band, ultrapure blue thermally activated delayed fluorescence (TADF) materials is extremely important for developing highly efficient organic light-emitting diodes (OLEDs). Here, spin–vibronic coupling (SVC)-assisted ultrapure blue emitters obtained by joining two carbazole-derived moieties at a *para* position of a phenyl unit and performing substitutions using several blocking groups are presented. Despite a relatively large singlet–triplet gap ( $\Delta E_{ST}$ ) of  $>0.2$  eV, efficient triplet-to-singlet crossover can be realized, with assistance from resonant SVC. To enhance the spin crossover, electronic energy levels are fine-tuned, thereby causing  $\Delta E_{ST}$  to be in resonance with a triplet–triplet gap ( $\Delta E_{TT}$ ). A sizable population transfer between spin multiplicities ( $>10^3$  s $^{-1}$ ) is achieved, and this result agrees well with theoretical predictions. An OLED fabricated using a multiple-resonance-type SVC-TADF emitter with CIE color coordinates of (0.15, 0.05) exhibits ultrapure blue emissions, with a narrow full-width-at-half-maximum of 21 nm and a high external quantum efficiency of 23.1%.

## 1. Introduction

According to spin statistics obtained under electrical excitation,<sup>[1]</sup> the generation of non-radiative triplet excitons is thrice that of radiative singlet excitons. Therefore, a major challenge in designing organic light-emitting diode (OLED) emitters that can achieve 100% internal quantum efficiency (IQE) has been the conversion of both the types of excitons to radiative photons.<sup>[2]</sup> Facile intra-molecular lowest-energy triplet–singlet ( $T_1$ – $S_1$ ) inter-conversion is one potential solution to this problem. Thermally activated delayed fluorescence (TADF), which permits 100% IQE of singlet emission through triplet-to-singlet reverse inter-system crossing (RISC), has emerged as a promising alternative to the more traditional phosphorescence, which is mediated by the large spin–orbit coupling (SOC) of precious


metals.<sup>[3]</sup> Naturally, a decisive parameter governing TADF performance is the  $S_1$ – $T_1$  energy gap ( $\Delta E_{ST}$ ), which, according to a simple two-state model,<sup>[4]</sup> is related to the exchange interaction  $K$  between electrons in the highest-occupied molecular orbital (HOMO) and the lowest-unoccupied molecular orbital (LUMO) according to the relationship  $\Delta E_{ST} \approx 2K$ .

Nascent TADF emitters adopted a donor–acceptor (DA)-type molecular design aimed at spatially separating the frontier orbitals because in such molecules, the HOMO and LUMO reside on the donor and acceptor moieties, respectively, thereby reducing  $K$  and  $\Delta E_{ST}$ .<sup>[5]</sup> Although a small  $\Delta E_{ST}$  of  $<0.1$  eV and a high RISC rate ( $k_{RISC}$ ) of the order of  $10^6$  s $^{-1}$  can be realized, the unavoidable charge-transfer character of the emissive  $S_1$  state generates a broad-band emission feature, resulting in low color purity, typically with a full-width-at-half-maximum (FWHM) of  $>50$  nm.<sup>[6]</sup> Thus, for display applications, a narrow-band color filter needs to be coupled to selectively transmit a primary color, thus impairing the light extraction efficiency. A recently developed molecular design concept based on the multiple-resonance (MR) effect has shown great potential for the remediation of such

V. V. Patil, H. L. Lee, K. H. Lee, W. J. Chung, J. Y. Lee  
School of Chemical Engineering  
Sungkyunkwan University  
Suwon 16419, Korea  
E-mail: leej17@skku.edu

I. Kim, W.-J. Son  
Data and Information Technology Center  
Samsung Electronics  
Hwaseong 18448, Korea

J. Kim, S. Park, H. Choi, S. O. Jeon  
Samsung Advanced Institute of Technology  
Samsung Electronics  
Suwon 16678, Korea  
E-mail: so.jeon@samsung.com

 The ORCID identification number(s) for the author(s) of this article can be found under <https://doi.org/10.1002/advs.202101137>

© 2021 The Authors. Advanced Science published by Wiley-VCH GmbH. This is an open access article under the terms of the Creative Commons Attribution License, which permits use, distribution and reproduction in any medium, provided the original work is properly cited.

DOI: 10.1002/advs.202101137

a broad emission band by judiciously placing electron-donating atoms and electron-accepting atoms in such a manner that the distributions of the frontier orbitals alternate within a rigid  $\pi$ -conjugation scaffold to realize a short-range charge transfer (CT). Consequently, in MR-TADF emitters, a narrow-banded spectrum with FWHM <30 nm can be simultaneously achieved along with reduced  $\Delta E_{ST}$ .

The design concepts of conventional MR-TADF emitters proposed so far require a combination of electron-deficient and electron-rich atoms such as boron–nitrogen (B/N),<sup>[7–11]</sup> boron–oxygen,<sup>[12,13]</sup> or carbonyl–nitrogen<sup>[14,15]</sup> within a polycyclic aromatic hydrocarbon (PAH) framework.<sup>[16]</sup> However, none of these PAH-type fluorescent emitters has achieved ultrapure blue color with a  $\gamma$ -color coordinate of 0.05 corresponding to the BT.2020 color standard established by the International Telecommunication Union.<sup>[17]</sup> 5,9-Diphenyl-5,9-diaza-13b-boranaphtho[3,2,1-de]anthracene (DABNA-1), which is a representative PAH material, offers an external quantum efficiency (EQE) of 13.5% with CIE color coordinates of (0.13, 0.09).<sup>[7]</sup> The linear extension of  $\pi$ -conjugation aids in improving efficiencies, but color purity is often compromised by red-shifted emission wavelengths.<sup>[9]</sup> *N,N*-dimethyl-9,9-dimethyl-5,5-diphenyl-5,9-dihydroquinolino[3,2,1-de]acridin-3-amine (DMACN-B) showing maximum EQE of 10% with CIE color coordinates of (0.151, 0.045) was also reported but still suffered from low EQE.<sup>[18]</sup> Therefore, the discovery of ultrapure blue emitters that have a novel core structure and can offer  $CIE_{\gamma} \approx 0.05$  and a theoretical maximum EQE of 20% (assuming an out-coupling efficiency of 20%) is a major challenge in the development of high-efficiency deep-blue OLEDs. Recently, we developed a narrow-band violet fluorescent emitter with  $CIE_{\gamma} = 0.018$  and FWHM = 14 nm by fusing indolo[3,2,1-jk]carbazole (ICz) with a carbazole unit and orienting the nitrogen atoms *meta* to the anchoring phenyl ring.<sup>[19]</sup> The emissive singlet exhibited the characteristics of an MR structure; however, the huge  $\Delta E_{ST}$  (as large as 0.44 eV) prevented the occurrence of TADF entirely, resulting in poor efficiency.

Here, we present spin–vibronic coupling (SVC)-assisted ultrapure blue TADF emitters based on indolo[3,2,1-jk]indolo[1',2',3':1,7]indolo[3,2-b]carbazole (BisICz), which was constructed by fusing an ICz unit with a carbazole unit through *para*-oriented nitrogen atoms. Both the  $S_1$  and  $T_1$  states of bare BisICz showed significant MR characteristics, and a reduced  $\Delta E_{ST}$  of approximately 0.3 eV was obtained from higher-level quantum chemical calculations and photophysical characterizations. Because of the non-negligibly large  $\Delta E_{ST}$  and insignificant  $S_1$ – $T_1$  SOC, the direct  $T_1 \rightarrow S_1$  population transfer was intrinsically hindered, and the second-order SVC played a crucial role in the spin crossover and even provided unique resonance conditions that enhanced RISC dynamics.<sup>[20,21]</sup> We demonstrated that the electronic energy levels could be fine-tuned by incorporating electron-donating groups into appropriate substitution sites on BisICz to induce resonant SVC and thereby achieve efficient RISC. Ultimately, we obtained new design principles for a high-efficiency deep-blue TADF emitter, which had an unprecedented CIE of (0.15, 0.05), a high EQE of 23.1%, and a small FWHM of 21 nm.

## 2. Results and Discussion

### 2.1. Molecular Design

We started with tri-phenyl amine (TPA) and constructed phenyl carbazole (PCz) and ICz by successively binding the adjacent phenyl rings into a planar structure (Figure 1). We employed a suitably high level of theory, SCS-ADC(2)/def2-SVP, which includes electron correlations in the form of double excitations to correctly predict energies and electron densities of excited states.<sup>[22,23]</sup> In this planarization of TPA, a decrease in  $\Delta E_{ST}$  corroborates well with an increase in the MR effect in the  $S_1$  state upon  $S_0$ – $S_1$  excitation by the alternating distributions of hole and particle densities, as shown in the difference density plot in Figure S1, Supporting Information. However, owing to the predominant local excitation of the  $\pi$ – $\pi^*$  character of the  $T_1$  state, whose level is stabilized by a large  $K$ ,  $\Delta E_{ST}$  remains significantly high (>0.5 eV), which prevents the realization of any meaningful RISC process. Moreover, even for ICz, the predicted wavelengths of singlet emission appear to be too short for it to be used as a blue emitter.

For triplet harvesting via RISC, not only should the  $S_1$  energy for ultrapure blue emission be reduced without disrupting the MR effect but the MR effect should also be sustained in the  $T_1$  state for a small  $\Delta E_{ST}$ . Therefore, we devised a new core named BisICz by fusing an ICz unit with a carbazole unit via the orientation of the nitrogen atoms *para* to the anchoring phenyl ring. In the case of the structural isomer of BisICz, wherein the nitrogen atoms were oriented to *meta* positions, a large  $\Delta E_{ST}$  of 0.44 eV was predicted because of the persistent  $\pi$ – $\pi^*$  character in the  $T_1$  state (Figure S2, Supporting Information). This result is in agreement with that of our previous experiment where no TADF activity was observed for 2,5,13,16-tetra-*tert*-butylindolo[3,2,1-jk]indolo[1',2',3':1,7]indolo[2,3-b]carbazole (tDIDCz).<sup>[19]</sup> In BisICz, although  $\Delta E_{ST}$  decreases to 0.33 eV compared to 0.56 eV for ICz, efficient spin crossover still remains a difficult challenge because the vibrational resonance mechanism of MR-TADF emitters operates at  $\Delta E_{ST} < 0.2$  eV, and hence, newer molecular design approaches are clearly needed. The existence of the close-lying  $T_2$  state with the  $T_1$ – $T_2$  energy gap ( $\Delta E_{TT}$ ) of 0.22 eV opens the possibility of engineering the energy levels required to optimize the resonance condition necessary for SVC-TADF emitters. Specifically,  $\Delta E_{ST}$  of BisICz should be reduced further by  $\approx 0.1$  eV.

Using quantum chemical methods, we performed a cursory survey on the substituent effect at the 3,6-positions of an isolated carbazole, which are well-known sites that affect the HOMO level and increase electrochemical stabilities.<sup>[24]</sup> Accordingly, two substituents were identified to have the ability to reduce  $\Delta E_{ST}$ . The addition of an electron-donating *tert*-butyl group to these sites destabilized the HOMO, whereas the addition of the phenyl group of a similar electron donor afforded the stabilization of the LUMO through the delocalization of a nitrogen lone pair (Table S1, Supporting Information).

Thus, we designed and synthesized three ultrapure blue emitters: BisICz, 2,5,11,14-tetrakis(1,1-dimethylethyl)indolo[3,2,1-jk]indolo[1',2',3':1,7]indolo[3,2-b]carbazole (tBisICz), and 2,5,11,14-tetrakis(3,5-di-*tert*-butylphenyl)-indolo[3,2,1-jk]indolo[1',2',3':

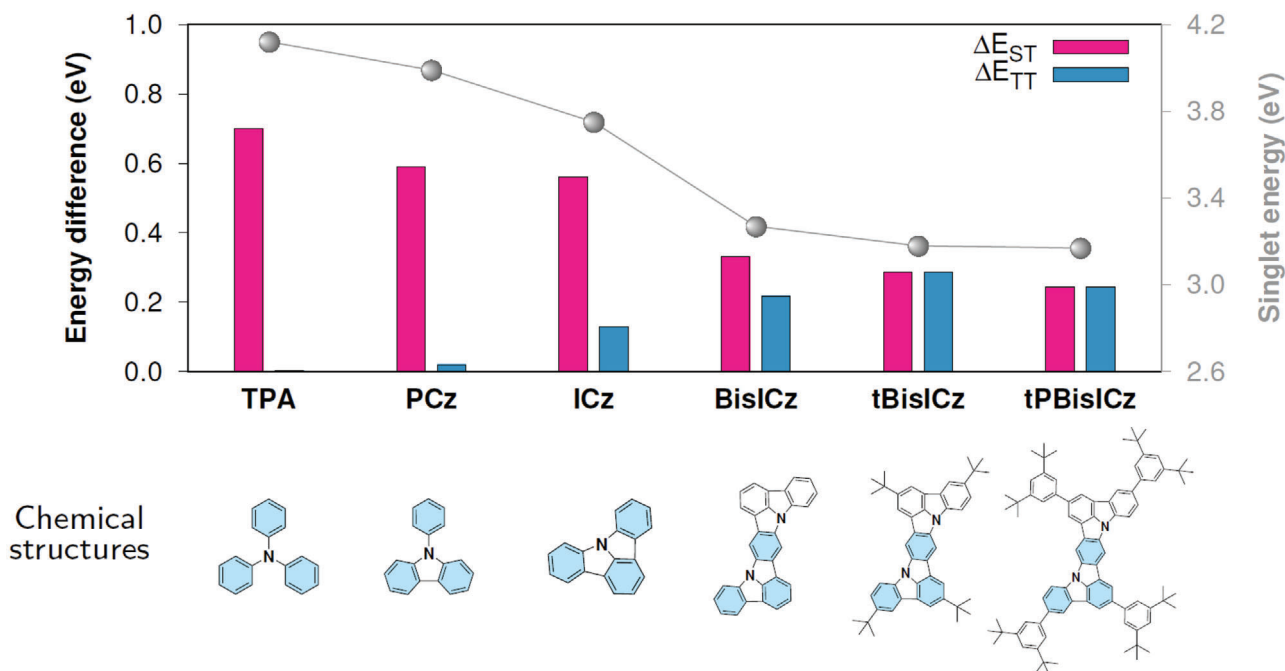


**Figure 1.** Molecular design. Chemical structures, energy differences,  $\Delta E_{ST}$  (adiabatic),  $\Delta E_{TT}$  (vertical), and singlet energy (vertical) of each molecule. The TPA cores are shaded in skyblue.  $\Delta E_{ST}$  and the singlet energy were calculated at the SCS-ADC(2) level, whereas  $\Delta E_{TT}$  was calculated at the  $\omega^*B97M-V$  level. The vertical energies were evaluated for the  $S_1$  geometry.

1,7]indolo[3,2-b]carbazole (tPBisICz) (Scheme S1, Supporting Information). Instead of adopting bare phenyl groups, we used 3,5-di-*tert*-butylphenyl groups to minimize undesirable molecular packing in the amorphous solid state encountered in the emissive layer of OLED. For a rigid narrow-band MR emitter with a large  $\Delta E_{ST}$ , achieving a small energy denominator associated with an on-resonance spin–vibronic (SV) model (Equation (2)) is essential for opening SVC-TADF materials for triplet harvesting. The energy denominator  $\Delta E_{TT} - \Delta E_{ST}$  for our emitters followed the order of BisICz (113 meV) > tBisICz (26 meV) > tPBisICz (6 meV). Based on these values, the latter two were considered to be suitable candidates for SVC-TADF emitters (Table S2, Supporting Information).

## 2.2. Resonant SVC

From a more fundamental perspective, the SV enhancement in the  $T_1$ – $S_1$  crossover is a second-order effect of an interaction Hamiltonian, which simultaneously considers the spin–orbit operator  $H^{\text{SO}}$  and non-Born–Oppenheimer operator  $H^{\text{nBO}}$ , thereby introducing the possibility of a strong inter-state vibronic coupling. The coupling matrix element up to the second order can be expressed as<sup>[25,26]</sup>

$$H_{ST} = \underbrace{H_{ST}^{\text{SO}}}_{\text{DSO}} + \frac{1}{2} \sum_{T'} H_{ST'}^{\text{SO}} H_{T'T}^{\text{nBO}} \left( \frac{1}{E_{T'} - E_T} + \frac{1}{E_{T'} - E_S} \right) \quad (1)$$

We immediately recognized two types of spin crossover interactions: the direct spin–orbit (DSO) coupling, which is governed by the electronic characters of the involved states, and the

SVC, which interacts with the SOC between the singlet and triplet states within the triplet manifold. To ensure pragmatic clarity in the following discussion on particular resonance conditions, we have deliberately excluded an additional SV term with mediating states in the singlet manifold. However, this term is considered in our quantitative analysis on RISC dynamics. We have also omitted index 1 of the  $S_1$  and  $T_1$  states for simplicity.

**Figure 2** illustrates a viable SV RISC pathway enhanced by resonance conditions for SVC-TADF emitters. In MR-TADF emitters, the  $S_1$  and  $T_1$  states have an identical electronic nature, which can be described as a short-range CT, and according to the El-Sayed rule,<sup>[27]</sup> the SOC between these states is insignificant. A recent work elucidated the RISC mechanism behind the excellent B/N-configuration emitters<sup>[28]</sup>: when the frequency of a vibration-inducing non-adiabatic coupling (NAC) between  $T_1$  and higher-lying  $T_n$  states matches  $\Delta E_{ST}$ , an SVC can accelerate the RISC process dramatically. The successive and continuous occurrence of such vibrational modes necessitates a resonantly enhanced RISC over a wide range of  $\Delta E_{ST}$ . Nevertheless, such resonance enhancement is inevitably terminated by the absence of vibrational modes >0.2 eV, except in the case of hydrogen stretching modes, which exhibit negligible NAC. Although emitters with large gaps (>0.2 eV) are not very promising, they can, in principle, be brought under resonance for second-order RISC by utilizing the energetic resonance between the  $T_2$  and  $S_1$  states based on the SVC expressed in Equation (1). The  $T_2$  state then provides the largest contribution to the sum-over-states expansion, and Equation (1) can be largely approximated as

$$H_{S_1T_1} \approx \frac{1}{2} \frac{H_{S_1T_2}^{\text{SO}} H_{T_2T_1}^{\text{nBO}}}{\Delta E_{TT} - \Delta E_{ST}} \quad (2)$$

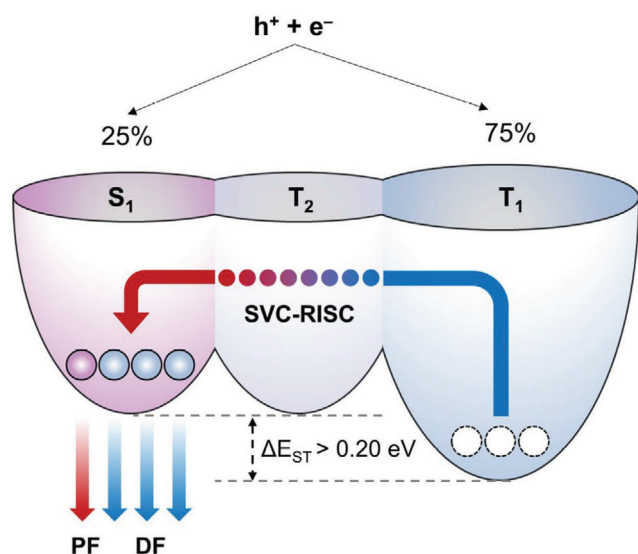


**Figure 2.** SVC-TADF mechanism. Schematic diagram of triplet harvesting of electro-generated excitons by TADF via on-resonance SVC.  $h^+$ , hole;  $e^-$ , electron; PF, prompt fluorescence; DF, delayed fluorescence; RISC, reverse inter-system crossing.

where  $\Delta E_{TT} = E_{T2} - E_{T1}$ . The above resonance condition requires a novel molecular core that is different from that of conventional B/N analogues because the succeeding  $T_2$  state is often found to be significantly higher in energy than the  $S_1$  state; for instance,  $\Delta E_{TT} = 0.59$  eV for DABNA-1.<sup>[24]</sup> Therefore, the resonance condition in Equation (2) cannot be employed. This resonance condition is also impractical for DA-type molecules. For instance, when the nearly degenerate CT states are higher in energy than the  $^3LE$  state, the above resonance condition may nearly be satisfied. However, the resonance enhancement vanishes simply because of the small SOC between the CT states, and instead, RISC occurs through the El-Sayed-allowed direct SOC between the  $^1CT$  and  $^3LE$  states if  $\Delta E_{ST}$  is sufficiently small.

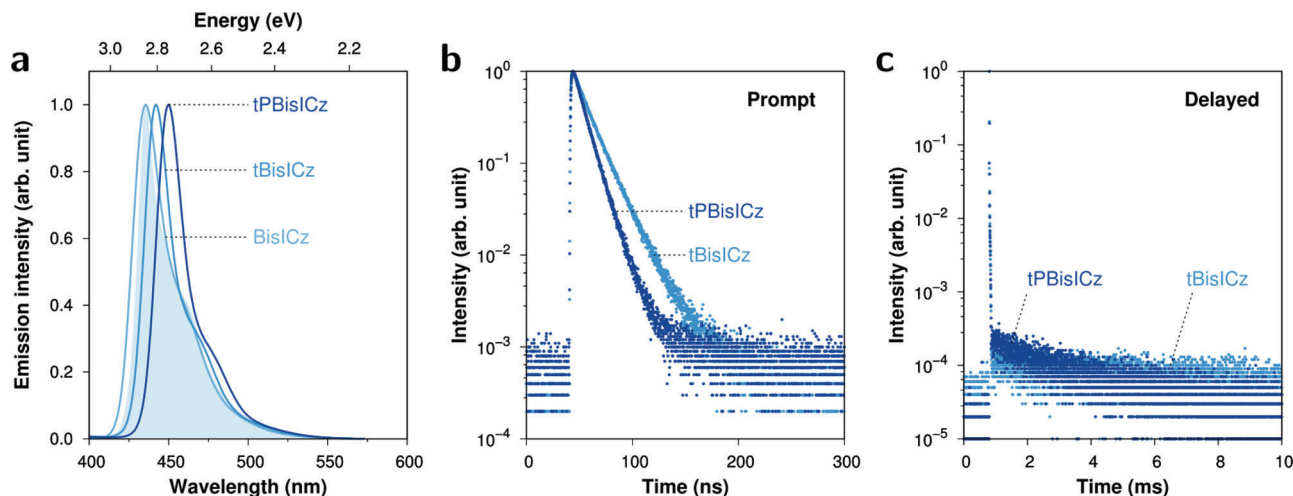
### 2.3. Photophysical Properties

Table S3, Supporting Information, summarizes the measured and calculated photophysical properties of BisICz-based compounds. Photophysical measurements were performed in diluted dichloromethane and in a thin film state using a high-triplet-energy mixed host, that is, 1,3-di(9H-carbazol-9-yl)benzene (mCP):diphenyl(4-(triphenylsilyl)phenyl)-phosphine oxide (TSPO1) (50:50). A low doping concentration of 1 wt% was used because fused planar ring compounds have the tendency to show aggregation in the solid state. The ultraviolet–visible (UV–vis) absorption spectra of the compounds (Figure S3a, Supporting Information) were similar, but the well-resolved and sharp absorption bands observed in the BisICz and tBisICz emitters were red-shifted in the tPBisICz emitter by the phenyl substituent, which extended the  $\pi$ -conjugation. The absorption bands below 370 nm are assigned to the  $\pi$ - $\pi^*$  transitions of the fused molecular structure,<sup>[29]</sup> whereas those between 370 and 450 nm are attributed to the  $n$ - $\pi^*$  transitions of the ICz part.<sup>[30]</sup>

Optical gaps were evaluated from absorption onsets of 2.84, 2.79, and 2.72 eV for BisICz, tBisICz, and tPBisICz, respectively.

The photoluminescence (PL) spectra of the emitters were collected from the thin films (Figure 3a). The solution spectra are shown in Figure S3b–d, Supporting Information. The peak wavelengths of the film/solution PL spectra were 436/432, 442/442, and 450/448 nm for BisICz, tBisICz, and tPBisICz, respectively. The small red shift of the PL emission in the tBisICz and tPBisICz emitters was attributed to the electron-donating substituents present in their structures; in particular, an ideal wavelength for ultrapure blue emission centered at 450 nm was obtained for tPBisICz. Owing to the rigid molecular structure based on the MR effect, the solid PL emission of BisICz was characterized by a small FWHM of 27 nm, whereas those of tBisICz and tPBisICz were characterized by an even smaller FWHM of 21 nm. Furthermore, BisICz and tBisICz showed similar Stokes shifts of 18 nm, whereas tPBisICz exhibited an even smaller Stokes shift of 13 nm. The small Stokes shift of the compounds points indeed to the rigidity of the coplanar molecular backbone structures due to MR effects. The Stokes shifts of the present emitters are significantly smaller than those of B/N-based MR-TADF emitters.<sup>[7]</sup> The fluorescence spectra of the emitters in the mCP:TSPO1 film did not differ significantly from those in the dilute solution, which partly implies an efficient energy transfer from the host to our emitter. The small red shift of 6 nm can be ascribed to the stabilization of the emissive state by the host polarity under the amorphous film condition. The  $E_s/E_T/\Delta E_{ST}$  values were obtained as 2.89/2.58/0.31, 2.84/2.55/0.29, and 2.81/2.54/0.27 eV for BisICz, tBisICz and tPBisICz, respectively. The PL emission hardly changed in different solvents, implying that the singlet emission had hardly any CT character (Figure S4, Supporting Information).

Excellent PL quantum yield (PLQY) values of 95% and 91% were obtained for tBisICz and tPBisICz. A slightly lower value (81%) was obtained for BisICz presumably because of molecular aggregation. We observed short nanosecond decay for prompt fluorescence (Figure 3b) and significant decay for delayed fluorescence from tBisICz and tPBisICz, as indicated by the slow decay in the transient PL data (Figure 3c) and by the large delayed PLQY ( $\Phi_{DF}$ ) values of 47% and 56%, respectively, which affirmed our design strategy for SVC-TADF emitters. From recent report by Lian Duan's group, it was described that tBisICz did not show TADF properties.<sup>[31]</sup> However, from temperature-dependent transient PL, tBisICz and tPBisICz showed increased delayed component by thermal activation, indicating that both emitters showed TADF phenomenon (Figure S5, Supporting Information). No delayed fluorescence was detected for BisICz (Figure S6, Supporting Information). From the prompt and delayed spectra measurement, tBisICz and tPBisICz showed delayed emission spectra, however, BisICz did not show any delayed emission (Figure S7, Supporting Information). The experimentally estimated  $k_{RISC}$  followed the inverse of the energy denominator  $\Delta E_{ST} - \Delta E_{TT}$ , as expected in the on-resonance SV model. We found that the radiative decay rates increased with the substitutions; the  $k_{PF}$  values were 5.4, 6.3, and  $9.2 \times 10^7$  s<sup>-1</sup> for BisICz, tBisICz, and tPBisICz, respectively; these values are in agreement with the theoretical predictions obtained for increasing oscillator strengths (Table S4, Supporting Information). Full details with fitting data are summarized in Table S5, Supporting Information. The thermal stability of the



**Figure 3.** Photophysical properties of BisICz-based emitters in 1 wt%-doped mCP:TSPO1 film at 300 K. a) Steady-state fluorescence spectra. Franck-Condon simulation of  $S_1 \rightarrow S_0$  emission for BisICz (filled curve; red-shifted by 6 nm). b,c) PL transient decay curves for (b) prompt and (c) delayed components. The corresponding plots for BisICz are given in Figure S6, Supporting Information, and no delayed component was observed.

emitters was determined by thermogravimetric analysis (TGA). The decomposition temperature ( $T_d$ ) with a 5% weight loss for tPBisICz was estimated to be 522 °C by TGA (Figure S8, Supporting Information). Hence, tPBisICz shows higher thermal stability than BisICz (424 °C) and tBisICz (435 °C) because of the bulky di-*tert*-butylphenyl substituent and can be safely evaporated in a vacuum evaporator.

## 2.4. RISC Dynamics

To further elucidate the resonance condition that transformed a formerly pure fluorescent emitter BisICz into an SVC-TADF emitter, we employed Fermi's golden rule in conjunction with the second-order coupling (Equation (1)) for the quantitative analysis of  $k_{\text{RISC}}$ :

$$k_{\text{RISC}} = \frac{2\pi}{\hbar} \sum_{\nu\nu'} P_{\nu}(T) |H_{\text{ST}}|^2 \delta(-\Delta E_{\text{ST}} + E_{\nu} - E_{\nu'}) \quad (3)$$

Here, the  $\delta$ -function imposes energy conservation on the  $T_1$  and  $S_1$  vibrational energies  $E_{\nu}$  and  $E_{\nu'}$  and the Boltzmann distribution  $P_{\nu}$  describes the thermal population at temperature  $T$ . Because the DSO and SV terms in Equation (1) cannot mix (up to the second order) in the square of the coupling because of time-reversal symmetry,<sup>[32]</sup>  $k_{\text{RISC}}$  simply becomes a sum of  $k_{\text{DSO}}$  and  $k_{\text{SV}}$  from the respective squared terms. The calculated  $k_{\text{RISC}}$  values are listed in Table S2, Supporting Information, together with other related excited-state properties.

Our computed  $k_{\text{RISC}}$  values of 1.47 and  $0.27 \times 10^3 \text{ s}^{-1}$  agree well quantitatively with the experimental values of 1.41 and  $0.15 \times 10^3 \text{ s}^{-1}$  for tPBisICz and tBisICz, respectively, measured under the thin film condition (Table S4, Supporting Information). Despite the similar  $\Delta E_{\text{ST}}$  values for tPBisICz and tBisICz, the smaller energy denominator  $\Delta E_{\text{ST}} - \Delta E_{\text{TT}}$  in the former ( $48 \text{ cm}^{-1}$ ) amplifies the electronic coupling dramatically and causes the rate constant of the former to be an order of magnitude

greater than that of the latter. As anticipated from the combination of the small  $S_1-T_1$  SOC and large  $\Delta E_{\text{ST}}$ , the RISC dynamics is completely governed by the SVC, that is,  $k_{\text{SV}}/k_{\text{RISC}} \approx 1.0$  (Table S2, Supporting Information). Because of the larger mismatch between  $\Delta E_{\text{ST}}$  and  $\Delta E_{\text{TT}}$ , a negligibly small  $k_{\text{RISC}}$  was obtained for BisICz. Detailed calculation methods of the rate constants are in the Supporting Information.

In all the emitters, the  $S_1-T_2$  SOC, which plays a crucial role in the second-order RISC, is a few times larger than the  $S_1-T_1$  SOC. Specifically, the product of the  $S_1-T_2$  SOC and  $T_1-T_2$  NAC is a decisive factor, and therefore, we now focus on the mode-wise deconvolution of  $k_{\text{RISC}}$  (Figure S9a, Supporting Information). We first project the non-adiabatic components onto the vibrational modes. By visually inspecting the NAC vectors between the  $T_1$  and  $T_2$  states (Figure S9b, Supporting Information), one can expect that the modes making major contributions in the SVC-RISC will be characterized as the stretched parts of the central benzene ring of the BisICz unit, which is distributed over four vibrational modes (Figure S9c, Supporting Information). The  $k_{\text{SV}}$  values arising from these modes account for  $\approx 50\%$  of the total  $k_{\text{RISC}}$  (Table S2, Supporting Information). Furthermore, another important factor for the SVC-RISC dynamics is the geometrical displacement between the  $S_1$  and  $T_1$  states. We varied the displacement by a factor of two in our SV model and observed that the enhancement in  $k_{\text{SV}}$  is effectively quenched, indicating that the resonance in the electronic coupling becomes diluted, which is partly related to the poor vibrational overlap (Figure S9d,e, Supporting Information).

To understand how these key vibrations allow a strong non-adiabatic mixing between the  $T_1$  and  $T_2$  states, we examined the natural transition orbitals (NTOs) of the involved states (Figure 4a). The same particle wavefunction is rendered for the  $S_1$ ,  $T_1$ , and  $T_2$  states. The hole wavefunctions of the  $S_1$  and  $T_1$  states are identical, whereas those of the  $T_1$  and  $T_2$  states differ, reflecting the NAC vectors to some extent. The hole wavefunction of  $T_2$  is localized in the Ph-Ph-Ph segment. This suggests that lowering the  $T_2$  state may not enhance the resonance observed

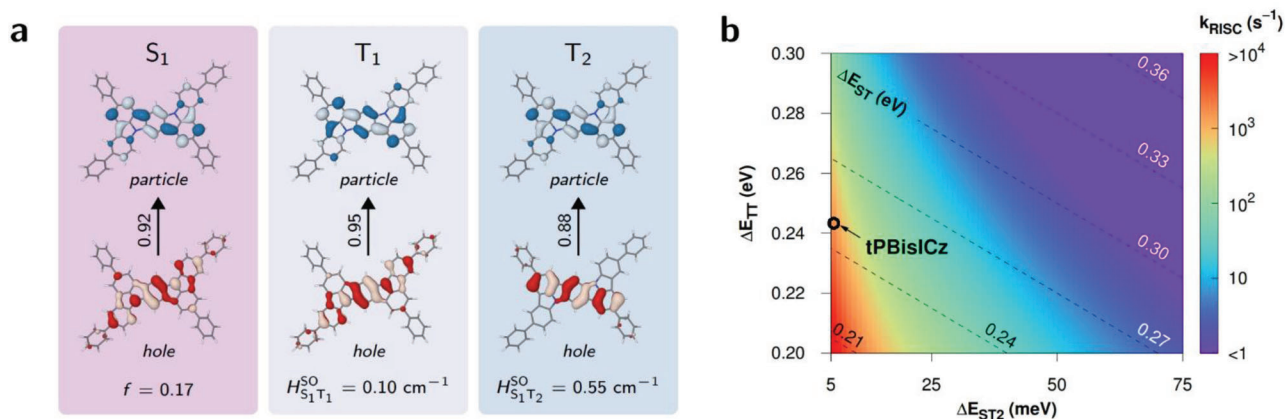


**Figure 4.** Molecular factors affecting  $k_{RISC}$ . a) NTO pairs for excited states of tPBisICz. The weights are given beside the arrows. The oscillator strength and SOCs are given for the singlet and triplet states, respectively. b)  $k_{RISC}$  simulated as a function of  $\Delta E_{TT}$  and  $\Delta E_{ST2}$  ( $\equiv |\Delta E_{TT} - \Delta E_{ST}|$ ) for tPBisICz. The diagonal scale of  $\Delta E_{ST}$  is also supplemented.

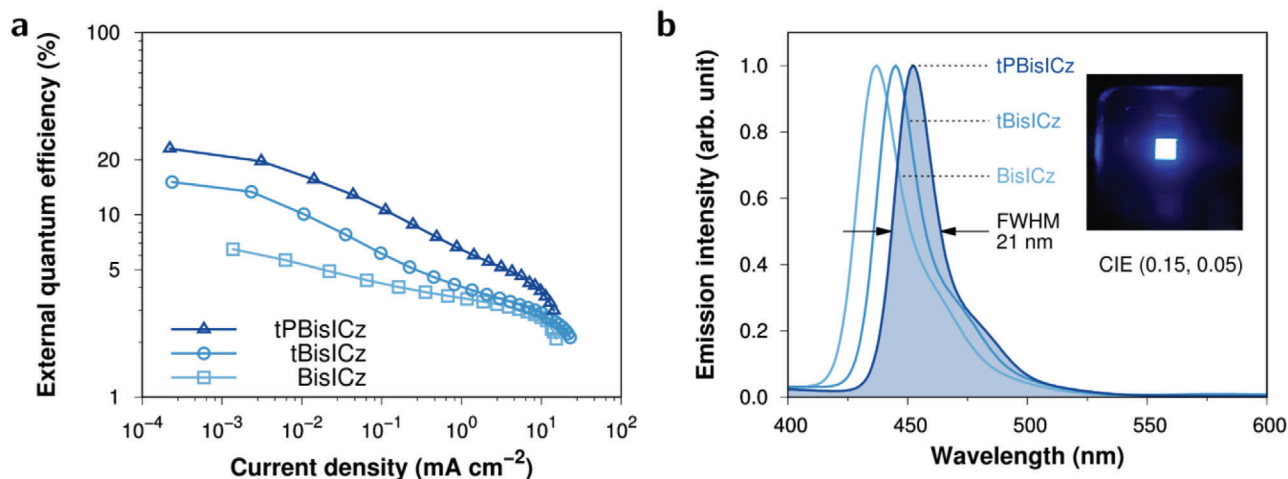


**Figure 5.** OLED performance of 1 wt%-doped mCP:TSPO1 devices. a) EQE versus current density. b) Normalised EL spectra. The inset shows the EL of the device fabricated using tPBisICz (corresponding to the filled curve).

here because this will start to perturb the  $T_1$  state with inevitable state mixing, leading to geometrical displacement in the central phenyl ring and consequent quenching of the SVC-RISC process.

Figure 4b shows how SVC-RISC enhancement varies with respect to the energy differences between the  $S_1$ ,  $T_1$ , and  $T_2$  states using the molecular properties of tPBisICz. To gain a sizable enhancement in  $k_{RISC}$ , simultaneous optimization should be carried out in all the three states such that  $\Delta E_{ST} \leq 0.26$  eV and  $|\Delta E_{ST} - \Delta E_{TT}| \leq 10$  meV, which will ensure that  $k_{SV} \approx 10^3 \text{ s}^{-1}$ . This is important because the present mechanism provides a new pathway for triplet harvesting in rigid emitters with large  $\Delta E_{ST}$ .

## 2.5. OLED Device Characterization

We demonstrated the potential of the ultrapure blue molecules as emitter materials in vacuum-deposited OLEDs using the device structure in Figure S10, Supporting Information. The energy lev-

els were measured by cyclic voltammetry, as detailed in Section S1.3.1, Supporting Information. The emissive layer consisted of the mCP:TSPO1 mixed host doped with ultrapure blue SVC-TADF emitters at a concentration of 1 wt%. The resulting electroluminescence (EL) performances are presented in Figure 5 and Table S6, Supporting Information. The EL spectra were almost identical to the respective PL spectra (Figure 3a) both in terms of the peak maximum and FWHM, clearly indicating the same emissive origin of the  $S_1$  state regardless of the exciton generation mechanism. These rule out the contribution of any bimolecular species such as exciplexes to the EL emission. The EL spectra were not changed according to voltage (Figure S11, Supporting Information). Strikingly, the device with tPBisICz showed excellent efficiencies with a maximum EQE of 23.1% (which is the theoretical maximum), current efficiency of  $13.5 \text{ cd A}^{-1}$ , and power efficiency of  $13.3 \text{ lm W}^{-1}$  (Figure S12, Supporting Information).  $\text{EQE}_{\text{max}}$  values followed the order of tPBisICz > tBisICz > BisICz. The EQE of the purely fluorescent BisICz device was low because

triplet excitons could not be utilized for singlet emission. The impressive performance of the OLED with tPBisICz suggests the almost complete triplet-to-singlet population transfer, assisted by the resonant SVC. The lower  $k_{\text{RISC}}$  of tBisICz competes with other non-radiative quenching processes such as triplet-triplet annihilation or triplet-polaron quenching, leading to the lower EQE. The high EQE of tPBisICz relative to that of tBisICz in spite of similar PLQY values was partly attributed to the high horizontal dipole orientation ratio, as shown in Figure S13, Supporting Information. As compared with the Lambertian distribution, the wide EL emission pattern from angle dependent EL measurement indicated that high EQE was not from microcavity or optical effect. (Figure S14, Supporting Information). Although the delayed fluorescence lifetime of the emitters is rather long in the sub-millisecond range, the triplet excited states of the emitters can be effectively managed using a suitable device structure, like the one employed in this work. The delayed fluorescence was clearly observed in the transient EL measurement (Figure S15, Supporting Information).

In all the OLEDs, irrespective of the efficiencies, an ultrapure blue CIE<sub>y</sub> coordinate of  $\leq 0.05$  was achieved. The EL spectra of these SVC-TADF-emitter-doped devices showed ultrapure emission with FWHM values as small as 21 nm. The color coordinates of the BisICz, tBisICz, and tPBisICz devices were (0.16, 0.04), (0.16, 0.05), and (0.15, 0.05), respectively. However, with the current device data, the efficiency roll-off is rather severe because of the lack of a highly stable device structure to accommodate high-energy triplet excitons and the annihilation of triplet excitons presumably due to a rather slow RISC conversion.

### 3. Conclusions

We designed ultrapure blue emitters with superior color purity based on an SV model, which was also used to elucidate the second-order RISC dynamics mediated by high-lying intermediary states and predominately driven by resonance conditions. Because of the energetic resonance between the involved states ( $S_1$  and  $T_2$ ) accompanied by large SOCs and non-Born–Oppenheimer couplings, resonance was realized by electron-donating substituents, thereby perturbing the frontier orbitals in a purely fluorescent BisICz molecule. The emitters (tBisICz and tPBisICz) showed a high PLQY (>90%), small Stokes shift (<20 nm), and narrow spectrum. The OLED fabricated using tPBisICz afforded a maximum EQE of 23.1%, a narrow FWHM of 21 nm, and an ultrapure blue color coordinate of (0.15, 0.05), which is very close to the industrial blue standard obtained without needing a narrow color filter. Such a high EL efficiency is mainly attributed to the kinetically slow but efficient RISC of the light emitting materials, which is, in turn, due to the resonance condition of the energy levels. The proposed principles offer a design strategy for large- $\Delta E_{\text{ST}}$  emitters, which were previously considered to be inoperable, by fine-tuning the electronic energy levels.

### Supporting Information

Supporting Information is available from the Wiley Online Library or from the author.

### Acknowledgements

This paper is based on work supported in part by the Samsung Advanced Institute of Technology (SAIT). J.Y.L. acknowledges support from a grant by the National Research Foundation of Korea (NRF-2020R1A2C2100872). Computational resources were provided by the Supercomputing Center of Samsung Electronics.

### Conflict of Interest

The authors declare no conflict of interest.

### Author Contributions

V.V.P., H.L.L., and I.K. contributed equally to this work. I.K. and W.-J.S. performed the theoretical calculations. V.V.P., H.L.L., and S.O.J. designed the molecules and assessed the synthetic feasibility of molecular candidates from the calculations. V.V.P. and H.L.L. synthesized the compounds and analyzed the chemical structures. S.O.J. and S.P. analyzed the spectroscopic data and electrochemical properties. K.H.L. and W.J.C. fabricated and tested the bottom-emitting devices and characterized the electrical and optical properties of the thin films. J.H.K. performed the anisotropic horizontal orientation study. S.O.J. and J.Y.L. wrote the first version of the manuscript. All the authors contributed to the discussion, writing, and editing of the manuscript. H.C. organized the project and supervised the computational chemistry study. J.Y.L. supervised the device fabrication and the project.

### Data Availability Statement

Research data are not shared.

### Keywords

blue organic light-emitting diodes, efficiency, narrow full-width-at-half-maximum, spin–vibronic coupling, Stokes shift

Received: March 20, 2021

Revised: June 24, 2021

Published online: August 13, 2021

- [1] M. A. Baldo, D. F. O'Brien, M. E. Thompson, S. R. Forrest, *Phys. Rev. B* **1999**, *60*, 14422.
- [2] M. A. Baldo, D. F. O'Brien, Y. You, A. Shoustikov, S. Sibley, M. E. Thompson, S. R. Forrest, *Nature* **1998**, *395*, 151.
- [3] H. Uoyama, K. Goushi, K. Shizu, H. Nomura, C. Adachi, *Nature* **2012**, *492*, 234.
- [4] H. Kaji, H. Suzuki, T. Fukushima, K. Shizu, K. Suzuki, S. Kubo, T. Komino, H. Oiwa, F. Suzuki, A. Wakamiya, Y. Murata, C. Adachi, *Nat. Commun.* **2015**, *6*, 8476.
- [5] X.-K. Chen, D. Kim, J.-L. Brédas, *Acc. Chem. Res.* **2018**, *51*, 2215.
- [6] Z. Yang, Z. Mao, Z. Xie, Y. Zhang, S. Liu, J. Zhao, J. Xu, Z. Chi, M. P. Aldred, *Chem. Soc. Rev.* **2017**, *46*, 915.
- [7] T. Hatakeyama, K. Shiren, K. Nakajima, S. Nomura, S. Nakatsuka, K. Kinoshita, J. Ni, Y. Ono, T. Ikuta, *Adv. Mater.* **2016**, *28*, 2777.
- [8] X. Liang, Z.-P. Yan, H.-B. Han, Z.-G. Wu, Y.-X. Zheng, H. Meng, J.-L. Zuo, W. Huang, *Angew. Chem., Int. Ed.* **2018**, *57*, 11316.
- [9] Y. Kondo, K. Yoshiura, S. Kitera, H. Nishi, S. Oda, H. Gotoh, Y. Sasada, M. Yanai, T. Hatakeyama, *Nat. Photonics* **2019**, *13*, 678.

- [10] Y. Xu, C. Li, Z. Li, Q. Wang, X. Cai, J. Wei, Y. Wang, *Angew. Chem., Int. Ed.* **2020**, *59*, 17442.
- [11] S. M. Suresh, E. Duda, D. Hall, Z. Yao, S. Bagnich, A. M. Z. Slawin, H. Bässler, D. Beljonne, M. Buck, Y. Olivier, A. Köhler, E. Zysman-Colman, *J. Am. Chem. Soc.* **2020**, *142*, 6588.
- [12] J. U. Kim, I. S. Park, C.-Y. Chan, M. Tanaka, Y. Tsuchiya, H. Nakanotani, C. Adachi, *Nat. Commun.* **2020**, *11*, 1765.
- [13] D. H. Ahn, S. W. Kim, H. Lee, I. J. Ko, D. Karthik, J. Y. Lee, J. H. Kwon, *Nat. Photonics* **2019**, *13*, 540.
- [14] X. Li, Y.-Z. Shi, K. Wang, M. Zhang, C.-J. Zheng, D.-M. Sun, G.-L. Dai, X.-C. Fan, D.-Q. Wang, W. Liu, Y.-Q. Li, J. Yu, X.-M. Ou, C. Adachi, X.-H. Zhang, *ACS Appl. Mater. Interfaces* **2019**, *11*, 13472.
- [15] Y. Yuan, X. Tang, X.-Y. Du, Y. Hu, Y.-J. Yu, Z.-Q. Jiang, L.-S. Liao, S.-T. Lee, *Adv. Opt. Mater.* **2019**, *7*, 1801536.
- [16] S. M. Suresh, D. Hall, D. Beljonne, Y. Olivier, E. Zysman-Colman, *Adv. Funct. Mater.* **2020**, *30*, 1908677.
- [17] *International Telecommunication Union*, Recommendation BT.2020 (08/2012), <https://www.itu.int/rec/R-REC-BT.2020-0-201208-S/en> (accessed: January **2020**).
- [18] A. Khan, X. Tang, C. Zhong, Q. Wang, S.-Y. Yang, F.-C. Kong, S. Yuan, A. S. D. Sandanayaka, C. Adachi, Z.-Q. Jiang, L.-S. Liao, *Adv. Funct. Mater.* **2021**, *31*, 2009488.
- [19] H. L. Lee, W. J. Chung, J. Y. Lee, *Small* **2020**, *16*, 1907569.
- [20] J. Gibson, A. P. Monkman, T. J. Penfold, *ChemPhysChem* **2016**, *17*, 2956.
- [21] M. K. Etherington, J. Gibson, H. F. Higginbotham, T. J. Penfold, A. P. Monkman, *Nat. Commun.* **2016**, *7*, 13680.
- [22] A. Pershin, D. Hall, V. Lemaire, J.-C. Sancho-Garcia, L. Muccioli, E. Zysman-Colman, D. Beljonne, Y. Olivier, *Nat. Commun.* **2019**, *10*, 597.
- [23] P. de Silva, *J. Phys. Chem. Lett.* **2019**, *10*, 5674.
- [24] Y. Zhang, D. Zhang, T. Tsuboi, Y. Qiu, L. Duan, *Sci. China: Chem.* **2019**, *62*, 393.
- [25] B. R. Henry, W. Siebrand, *J. Chem. Phys.* **1971**, *54*, 1072.
- [26] T. J. Penfold, E. Gindensperger, C. Daniel, C. M. Marian, *Chem. Rev.* **2018**, *118*, 6975.
- [27] M. A. El-Sayed, *J. Chem. Phys.* **1963**, *38*, 2834.
- [28] I. Kim, K. H. Cho, S. O. Jeon, W.-J. Son, D. Kim, Y. M. Rhee, I. Jang, H. Choi, D. S. Kim, *JACS Au* **2021**, <https://doi.org/10.26434/chemrxiv.12413417.v1>.
- [29] H. Li, Y. Wang, K. Yuan, Y. Tao, R. Chen, C. Zheng, X. Zhou, J. Li, W. Huang, *Chem. Commun.* **2014**, *50*, 15760.
- [30] P. Kautny, C. Zhao, D. Schopf, B. Stöger, E. Horkel, J. Chen, D. Ma, J. Föröhlich, D. Lumpi, *J. Mater. Chem. C* **2017**, *5*, 1997.
- [31] J. Wei, C. Zhang, D. Zhang, Y. Zhang, Z. Liu, Z. Li, G. Yu, L. Duan, *Angew. Chem., Int. Ed.* **2021**, *60*, 12269.
- [32] I. Kim, S. O. Jeon, D. Jeong, H. Choi, W.-J. Son, D. Kim, Y. M. Rhee, H. S. Lee, *J. Chem. Theory Comput.* **2020**, *16*, 621.